www.springer.com/41230
https://doi.org/10.1007/s41230-026-5146-x

Control of fine grain structures and strengthening-toughening mechanisms in magnesium alloys fabricated by wire-arc directed energy deposition

Wei Liu[1], ***Hai-long Jia**[1, 2], **Yi-hang Yang**[1], **Min Zha**[1], **Artem Marchenkov**[3], **Pin-kui Ma**[1], **and Hui-yuan Wang**[1, 2]

1. Key Laboratory of Automobile Materials of Ministry of Education & School of Materials Science and Engineering, Jilin University, Changchun 130025, China

2. International Center of Future Science, Jilin University, Changchun 130012, China

3. Moscow Power Engineering Institute, National Research University, Moscow 111250, Russia

Copyright © 2026 Foundry Journal Agency

Abstract: Wire-arc directed energy deposition (WA-DED) has attracted considerable attention for the fabrication of magnesium (Mg) alloys due to its high efficiency, low cost, and rapid prototyping capability for complex components. However, the inherent rapid solidification and complex thermal cycling associated with WA-DED often result in coarse columnar grains and pronounced mechanical anisotropy, which severely limiting its application potential. In this study, a novel spiral oscillation (SO) strategy was implemented during WA-DED AZ31 Mg alloy to refine the microstructure, reduce mechanical anisotropy, and achieve a strength-ductility synergy. Specifically, the yield strength (YS), ultimate tensile strength (UTS), and elongation (EL) are increased by 9.7%, 38.1%, and 147%, respectively. These improvements by the SO strategy are primarily attributed to the promotion of columnar-to-equiaxed transformation (CET), a 74.2% reduction in maximum texture intensity, and a more uniform distribution of second-phase particles. Second-phase particles are primarily composed of Al_8Mn_5 and Al_8Mn_4Y. This study provides a novel strategy for microstructural control aimed at improving the performance of WA-DED AZ31 Mg alloy components.

Keywords: magnesium alloy; wire arc directed energy deposition; spiral oscillation; isotropy; strength-ductility synergy

CLC numbers: TG146.22 **Document code:** A **Article ID:** 1672-6421(2026)03-367-10

1 Introduction

Magnesium alloys represent the lightest class of engineering structural materials, with a density of ~1.74 g·cm^{-3}, approximately 65% that of aluminum, 40% of titanium, and 25% of steel[1, 2]. Although the absolute tensile strength of Mg alloys is generally lower than of high-strength steels or certain aluminum alloys, their exceptionally low density results in a remarkably high specific strength and specific stiffness, which can exceed those of some aluminum alloys and steels. Furthermore, Mg alloys have excellent electromagnetic shielding capabilities and biodegradability, making them ideal for lightweight structural applications with significant potential in automotive, military equipment, aerospace and other fields[3-6].

However, conventional fabrication methods for Mg alloys, such as casting, forging, extrusion, and rolling, are often constrained by mold limitations. These processes are susceptible to metallurgical defects like porosity and generally struggle to directly form complex components. Moreover, the inherent hexagonal close-packed (HCP) crystal structure of Mg alloys results in low plasticity and poor formability at room temperature, which further limits the application of Mg alloys[7, 8]. Therefore, there is an urgent need to develop advanced manufacturing techniques capable of integrating complex geometries while mitigating the limitations of traditional processing routes.

Additive manufacturing (AM) is an emerging

***Hai-long Jia**

Ph. D. Professor. His research interests primarily focus on the structural control and processing technologies of high-performance light alloys.

E-mail: jiahailong@jlu.edu.cn

Received: 2025-07-02; Revised: 2026-01-18; Accepted: 2026-01-20

fabrication technique that builds components layer-by-layer along a predefined path, enabling the rapid prototyping of complex geometries[9]. Unlike traditional subtractive manufacturing methods, AM is not constrained by shape limitations, offering substantial potential for the fabrication of complex Mg alloy components. According to the type of heat source and raw materials, the most commonly used metal AM processes are categorized into three types: laser powder bed fusion (L-PBF), laser directed energy deposition (L-DED), and wire arc additive manufacturing (WAAM, also called wire arc directed energy deposition, WA-DED)[10]. However, the high laser reflectivity of Mg alloys, coupled with the high flammability and explosiveness of Mg alloy powders, introduces significant safety concerns in industrial applications[11]. These safety concerns severely limit the application of L-PBF and L-DED for Mg alloys. In contrast, WA-DED employs Mg alloy wire as raw material and an electric arc as the heat source, effectively eliminating powder-related safety hazards. This intrinsic safety advantage makes WA-DED a highly promising technology for the additive manufacturing of Mg alloys.

Depending on the welding process, WA-DED can be classified into gas metal arc welding (GMAW), gas tungsten arc welding (GTAW), and plasma arc welding (PAW), amongst others[12]. The primary process parameters in WA-DED include deposition current and deposition speed, both of which significantly affect the geometric formability and overall quality of deposited components. Previous studies indicate that a high deposition speed combined with a low deposition current can result in discontinuous deposits due to insufficient heat input and incomplete wire melting. Conversely, a low deposition speed combined with a high deposition current can lead to excessive material accumulation due to the slower movement of the deposition head[13]. Therefore, the optimization of these process parameters is essential to achieving high-quality deposition. In addition to improving deposition quality, optimized process parameters can promote grain refinement and reduce texture intensity[14]. However, grain coarsening is frequently observed with increasing build heights. This phenomenon is primarily attributed to the decreased heat dissipation efficiency and hindered thermal diffusion at greater heights, caused by cumulative heat input inherent to the layer-by-layer deposition process[15]. The variation in thermal cycling and heat accumulation at different build heights inevitably results in heterogeneous microstructural evolution throughout the component. Consequently, this microstructural heterogeneity leads to variations in mechanical properties. As reported in previous studies[7, 16], AZ31 Mg alloy components fabricated via WA-DED commonly exhibit coarse columnar grain structures, which result in pronounced mechanical anisotropy and limit their broader industrial applicability.

Currently, Mg alloys commonly employed in WA-DED include Mg-Al-Zn (AZ31[17-19], AZ61[20], AZ91[21]) and Mg-RE (Mg-Gd[22], Mg-Y[23]) alloys. Among these, Mg-Al-based alloys have been extensively studied, particularly the AZ31 Mg alloy. Research indicates that varying pulse frequencies during WA-DED can regulate grain structures[24]. AZ31 prepared via cold metal transfer (CMT)-WA-DED exhibits superior mechanical properties to castings, approaching those of forgings, while demonstrating better corrosion resistance than hot-rolled AZ31 sheets. However, mechanical properties of WA-DED AZ31 Mg alloys exhibit pronounced anisotropy[25]. Furthermore, by adjusting process parameters, favorable wettability and excellent forming morphology can be achieved with low equivalent heat inputs. Previous studies have shown that the columnar-to-equiaxed transition (CET) can be effectively controlled by adjusting the degree of undercooling, including compositional, thermal and curvature undercooling[26]. During the DED process, the primary methods currently employed for grain refinement to enhance mechanical properties include the application of external energy fields (e.g., ultrasonic vibration[27], cryogenic cooling[14], water cooling[16], etc.), the introduction of localized plastic deformation (e.g., via laser shock peening[28], ultrasonic rolling[29, 30], etc.), and the addition of heterogeneous nucleation particles[31]. Although these methods have demonstrated effectiveness in grain refinement and performance improvement, they are often limited by operational complexity, requiring additional specialized equipment.

Heat source oscillation has been widely applied in AM processes involving laser or laser-arc hybrid heat sources to promote grain refinement and enhance mechanical properties[32, 33]. However, in the context of WA-DED for Mg alloys, the feasibility of employing oscillation strategies, particularly through modifications of the deposition path, to influence microstructural evolution and mechanical performance remains insufficiently explored and warrants further investigation.

In this study, a spiral oscillation deposition strategy was introduced to enhance the conventional straight line deposition approach for WA-DED AZ31 Mg alloy. This strategy was designed to refine microstructures and improve mechanical properties of deposited components. The effects of SO strategy on grain size and morphology, second-phase distribution and composition, and mechanical performance were systematically investigated through electron backscatter diffraction (EBSD) and scanning electron microscopy (SEM) characterization. This work presents a novel processing route for WA-DED AZ31 Mg alloy, enabling grain refinement and the fabrication of high-performance Mg alloy components with isotropic mechanical properties.

2 Experimental

2.1 Material preparation

In this work, AZ31 Mg alloy wire (2.6 Al, 0.6 Zn, 0.5 Mn, 0.5 Sn, 0.01 Y, wt.%) with a diameter of 1.2 mm was used as the raw material. Deposition was carried out on rolled AZ31 Mg alloy substrates with dimensions of 200 mm×30 mm×4 mm (L×W×H) using the cold metal transfer wire-arc additive manufacturing (CMT-WAAM) system. A schematic of the deposition process is shown in Fig. 1(a). Two deposition paths were employed: straight line (SL) and spiral oscillation (SO), as illustrated in Fig. 1(b). The key process parameters included a deposition current of 110 A and a deposition speed of 5 mm·s^{-1}. For SO deposition, an oscillation amplitude of 4 mm and wavelength of 3 mm were applied. High-purity argon gas (99.99%) was used as the shielding atmosphere at a flow rate of 18–20 L·min^{-1}. To ensure thermal consistency between layers, inter-layer cooling to 50 °C was conducted before each subsequent deposition. Thin-walled components comprising ten layers were fabricated using these parameters with bidirectional deposition.

2.2 Microstructure characterization and property measurement

Microstructural characterization was performed using a Zeiss Sigma 500 scanning electron microscope (SEM) equipped with an Oxford Instruments NordlysNano AZtec electron backscatter diffraction (EBSD) detector and an X-MaxN AZtec energy dispersive spectroscopy (EDS) system. Sample cutting locations are shown in Fig. 1(c). For EBSD analysis, samples were electrolytically polished at 20 V for 40–45 s in a solution (800 mL ethanol, 100 mL propanol, 18.5 mL distilled water, 10 g hydroxyquinoline, 75 g citric acid, 41.5 g sodium thiocyanate, and 15 mL perchloric acid). The EBSD data acquisition step size was set to be 5 μm and the acquired data were analyzed using Channel 5 software. Tensile sample geometries and extraction locations are also shown in Fig. 1(c). Room-temperature tensile tests were carried out using a Shimadzu AGS-X universal testing machine at a constant crosshead speed of 0.6 mm·min^{-1}. In addition, precipitates in SL and SO components were investigated using transmission electron microscopy (TEM, Thermofisher Talos F200X). The TEM specimens were first ground to a thickness of approximately 80 μm using sandpaper and then thinned by ion milling.

3 Results and discussion

3.1 Mechanical properties

Figure 2(a) presents statistical histograms comparing mechanical properties of SL and SO deposited components. As shown in Fig. 2(a), mechanical properties of components deposited with the SO strategy are significantly improved. Taking the building direction (BD) as an example, the SL component shows yield strength (YS), ultimate tensile strength (UTS), and elongation (EL) values of 92 MPa, 168 MPa, and 6.6%, respectively. However, the SO component exhibits corresponding values of 101 MPa, 232 MPa, and 16.3% along BD. Compared to the SL component, the SO strategy results in YS, UTS, and EL improvements of 9.7%, 38.1%, and 147%, respectively. These results demonstrate that the SO strategy effectively enhances mechanical performance and achieves a synergistic improvement in both strength and ductility.

It is worth noting that the SL component exhibits pronounced mechanical anisotropy between BD and DD, whereas the SO component shows markedly improved isotropy. To facilitate a more intuitive comparison, the variance rates of mechanical properties between BD and DD were calculated, as shown in Fig. 2(b). As shown, the variance rates of YS, UTS, and EL between BD and DD decrease from 3.4%, 14.3%, and 36.4% in SL component to 1.0%, 0.4%, and 0.6% in SO component, respectively. These results clearly demonstrate that the SO strategy significantly enhances the isotropy of mechanical properties in WA-DED AZ31 Mg alloy component.

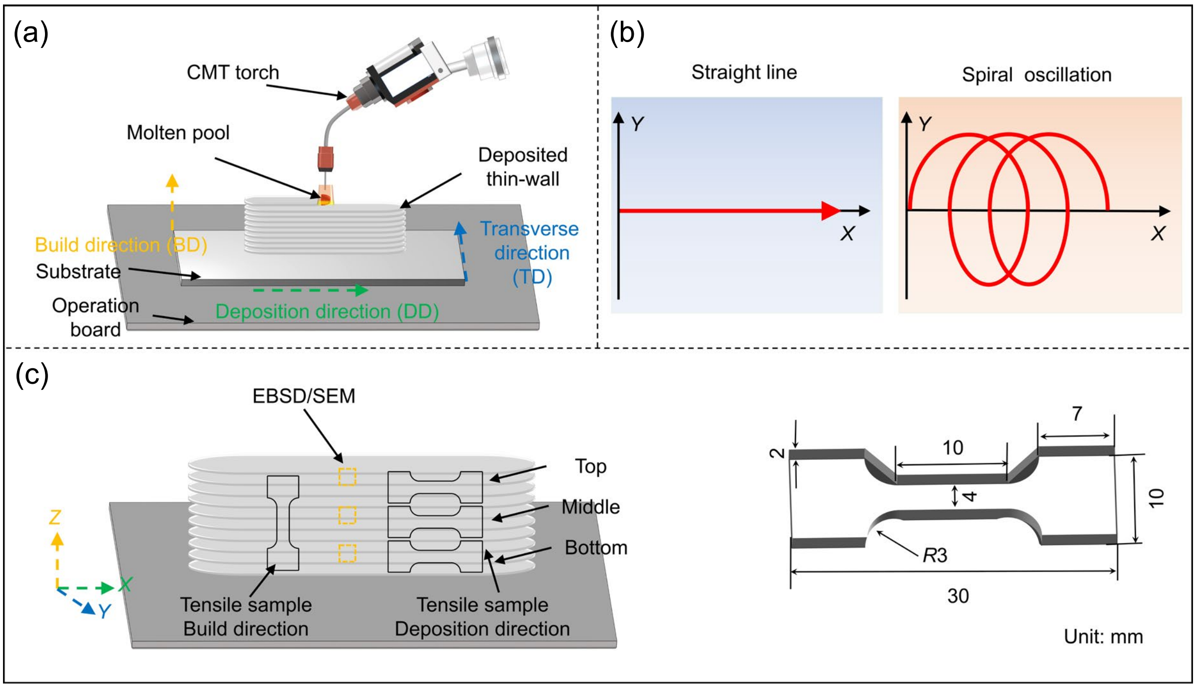

Fig. 1: Schematic of experimental process for WA-DED AZ31 Mg alloy components: (a) deposition process; (b) deposition path; (c) position and size of sample

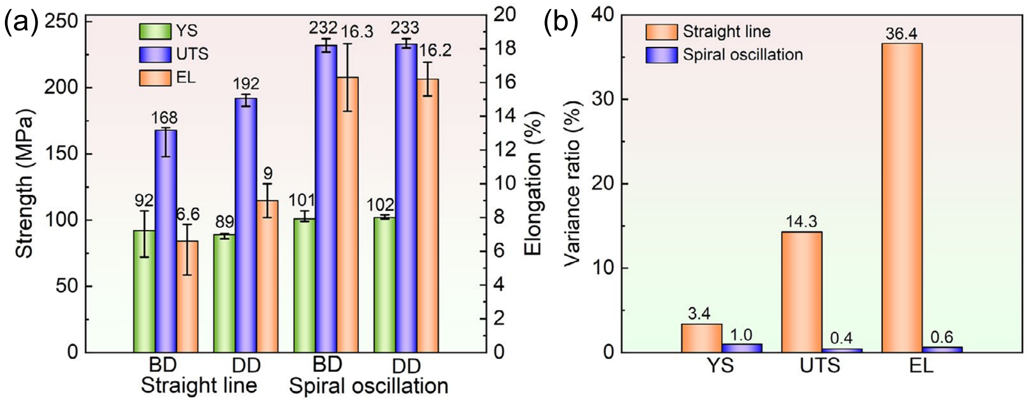

Fig. 2: Room temperature tensile property statistics: (a) performance statistics histogram; (b) histogram showing the variance ratio of mechanical properties between BD and DD

3.2 Grain morphology and texture analysis

EBSD analyses were performed on two deposited components to investigate the effects of deposition strategy on grain morphology and size distribution, as shown in Figs. 3 and 4, respectively. As illustrated in Fig. 3, grains at different locations of the SL component exhibit a microstructure comprising coarse columnar grains and fine grains, with a significant higher percentage of columnar grains. The average grain sizes of top, middle, and bottom regions are 99.1 μm, 93.7 μm, and 84.8 μm, respectively. It indicates a progressive increase in grain size with deposition heights. Furthermore, comparative analysis of EBSD IPF maps from bottom to top regions further reveals a distinct evolution in columnar grain morphology: the bottom region near the substrate contains finer grains, while the top region is dominated by coarser and fewer grains. This grain coarsening with increasing build heights is primarily attributed to changes in heat dissipation efficiency during the layer-by-layer deposition process[15]. Near the substrate, direct contact enables efficient heat extraction and rapid cooling, thereby restricting grain growth and promoting the formation of fine grains. As the deposition height increases, the heat dissipation path becomes longer and less efficient, reducing the cooling rate and allowing grains to grow more extensively. As a result, the upper regions of the SL component develop a microstructure dominated by coarse columnar grains.

As shown in Fig. 4, the microstructure of the SO component comprises a mixture of fine columnar grains and fine equiaxed grains uniformly distributed across all regions. In contrast to the SL strategy, the SO strategy significantly increases the proportion of equiaxed grains. The average grain sizes in the top, middle, and bottom regions of the SO component are 74.2 μm, 71.0 μm, and 69.8 μm, respectively. It exhibits a similar trend of increasing grain sizes with build heights. Additionally, EBSD IPF maps demonstrate a progressive increase in the fraction of coarse columnar grains along the deposition height from the bottom to top regions. Similar to the SL condition, this microstructural evolution is also governed

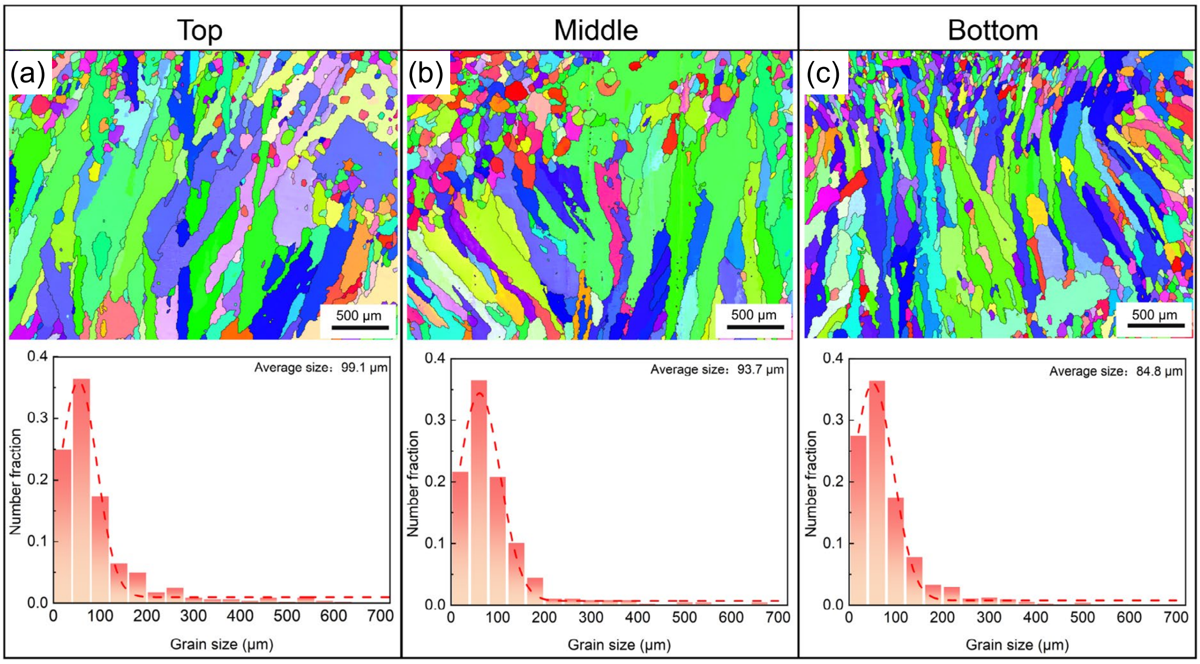

Fig. 3: IPF maps and grain size distribution histograms of different positions in SL component: (a) top; (b) middle; (c) bottom

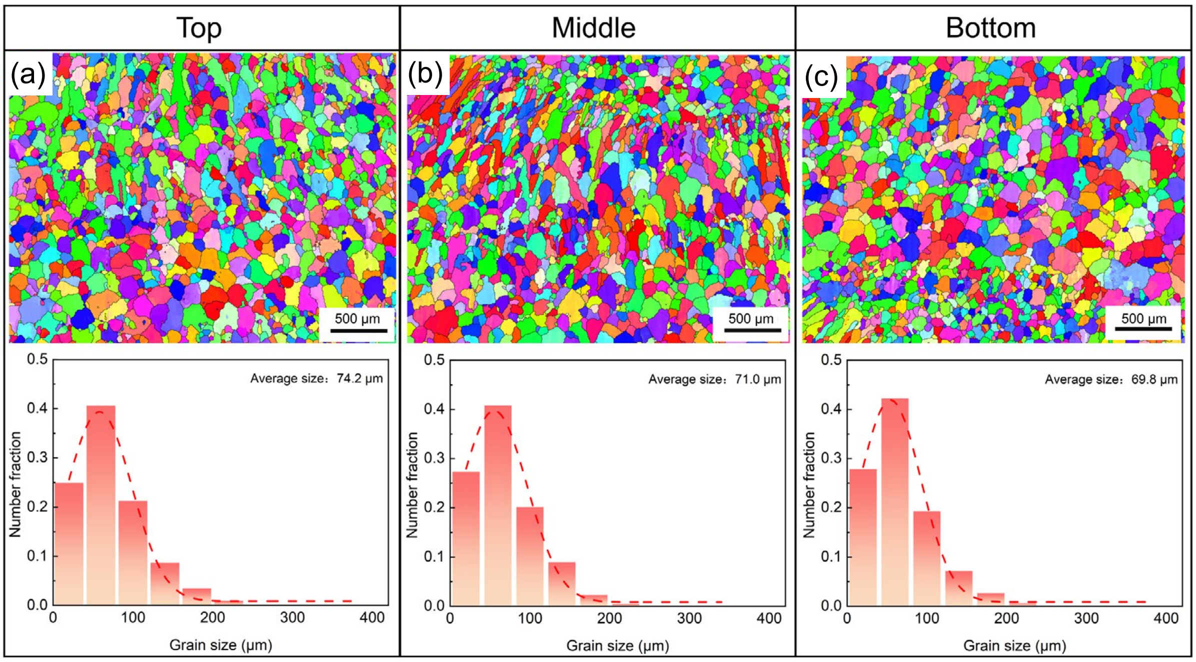

Fig. 4: IPF maps and grain size distribution histograms of different positions in SO component: (a) top; (b) middle; (c) bottom

by the progressive reduction in heat dissipation efficiency with increasing deposition heights[15].

Compared to the SL strategy, the SO strategy induces a clear microstructural transition from coarse columnar grains to fine equiaxed grains. Significant grain refinement is achieved in the top, middle, and bottom regions, with average grain size reductions of 24.9 μm (25.1%), 22.7 μm (24.2%), and 15.0 μm (17.7%), respectively. These results confirm that the SO strategy effectively refines the grain structure and promotes columnar-to-equiaxed transformation (CET). Grain refinement increases the density of grain boundaries, which act as barriers to dislocation motion and thus enhance the yield strength via the Hall-Petch relationship[34, 35]. Furthermore, while grain boundaries in coarse columnar structures can serve as preferential pathways for rapid crack propagation, the transition to equiaxed grains mitigates this tendency, thereby reducing susceptibility to premature fracture[31]. The uniform morphology of equiaxed grains also promotes uniform plastic deformation under applied loading. Collectively, these microstructural modifications including grain refinement, CET, and morphological homogenization contribute to the substantial improvements in mechanical properties observed in the SO component.

Pole figures for different positions of SL and SO components are shown in Figs. 5 and 6, respectively. As illustrated in Fig. 5, the maximum texture intensity in the SL component decreases progressively from 22.4 mrd at the top to 11.5 mrd in the middle and 9.3 mrd at the bottom. This trend is attributed to the microstructural evolution along the build height from a small number of large columnar grains in the upper regions to a higher density of smaller columnar grains near the substrate.

Figure 6 shows that the maximum texture intensity in the SO component decreases progressively from 3.1 mrd at the top to 2.9 mrd in the middle and 2.4 mrd at the bottom.

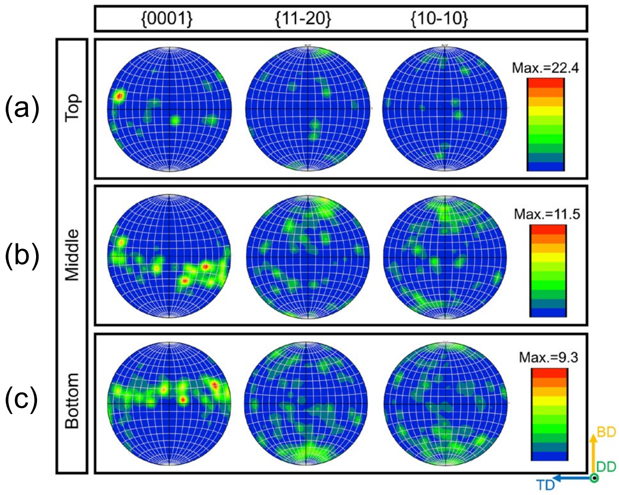

Fig. 5: Pole figures of different positions in SL component: (a) top; (b) middle; (c) bottom

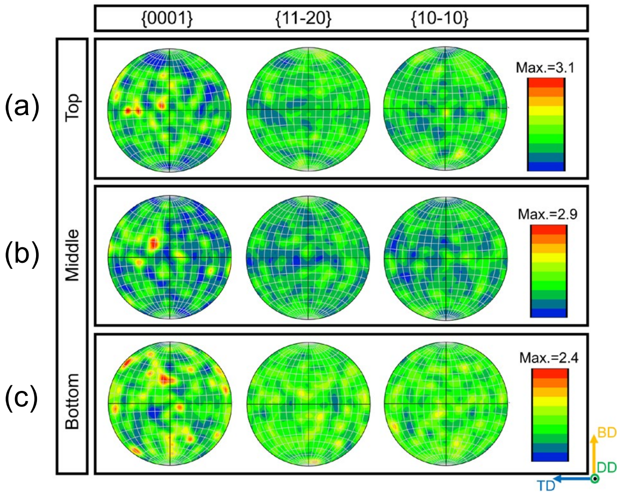

Fig. 6: Pole figures of different positions in SO component: (a) top; (b) middle; (c) bottom

Compared to the SL component, texture intensities in the SO component are significantly reduced. Specifically, maximum texture intensities at the top, middle, and bottom regions are decreased by 19.3 mrd (86.2%), 8.6 mrd (74.8%), and 6.9 mrd (74.2%), respectively. Furthermore, grains in the SO component exhibit predominantly random orientations, which is beneficial for reducing mechanical anisotropy of deposited components.

3.3 Second-phase evolution

Figure 7 presents SEM images of different regions in both SL and SO components. It can be observed that, for both deposition strategies, the size of second-phase particles increases progressively from bottom to top, with this trend being more pronounced in the SL component. This phenomenon is primarily attributed to the reduction in heat dissipation efficiency with increasing build heights. Furthermore, the second-phase distribution in the SO component is significantly more uniform compared to that in the SL component. The SO strategy facilitates the uniformity by disrupting the localized accumulation of second-phase particles, which helps to mitigate stress concentrations that typically act as sites for crack initiation. As a result, the more homogeneous second-phase distribution achieved by the SO strategy contributes to improved ductility and overall mechanical performance.

Figure 8 presents EDS analyses of middle regions in SL and SO components. From Fig. 8, it can be seen that second-phase particles are primarily enriched in Al and Mn elements. Point analyses of the second-phases in SL and SO components (Table 1) reveal that atomic ratios of Points 1 and 3 are similar to those of the Al_8Mn_5 phase, while atomic ratios of Points 2 and 4 are similar to those of the Al_8Mn_4Y phase. TEM characterization was carried out on both the SL and SO components to identify secondary phases (Fig. 9). EDS combined with selected area electron diffraction (SAED) reveals that secondary phases in both states are composed of Al_8Mn_5 and Al_8Mn_4Y. Importantly, the SO strategy uniforms the distribution of second-phase particles without changing their chemical composition. This suggests that improved mechanical properties observed in the SO component are attributed to changes in second-phase distribution and morphology, rather than the second-phase type.

It is evident that the SO strategy microstructures both in grain morphology and secondary phase distribution are entirely distinct from those generated by SL. This difference primarily arises from the intense molten-pool agitation and the reduced temperature gradient caused by SO[36, 37]. To facilitate understanding, schematics illustrating the flow field and grain structures within molten pools of SL and SO components are shown in Fig. 10. Compared to the SL mode, the oscillatory motion in the SO mode produces a larger number of complex and multidirectional vortices within the molten pool[37, 38]. The increased number and intensity of multidirectional vortices greatly enhance shear and fragmentation effects on columnar grains, thereby promoting significant grain refinement. The fragmented columnar grains subsequently serve as additional nucleation sites, further facilitating the formation of equiaxed grains. Moreover, vigorous fluid agitation improves solute mixing uniformity in the molten pool, leading to finer and more uniformly distributed secondary phases[37]. The intensified arc stirring increases the molten-pool velocity, which facilitates the escape of gas bubbles and thus reduces metallurgical defects such as porosity, leading to improved microstructural uniformity and mechanical properties[38]. Furthermore, the SO strategy effectively decreases the temperature gradient within the molten pool, thereby enhancing grain refinement[24]. The morphology of the solidified microstructure is mainly

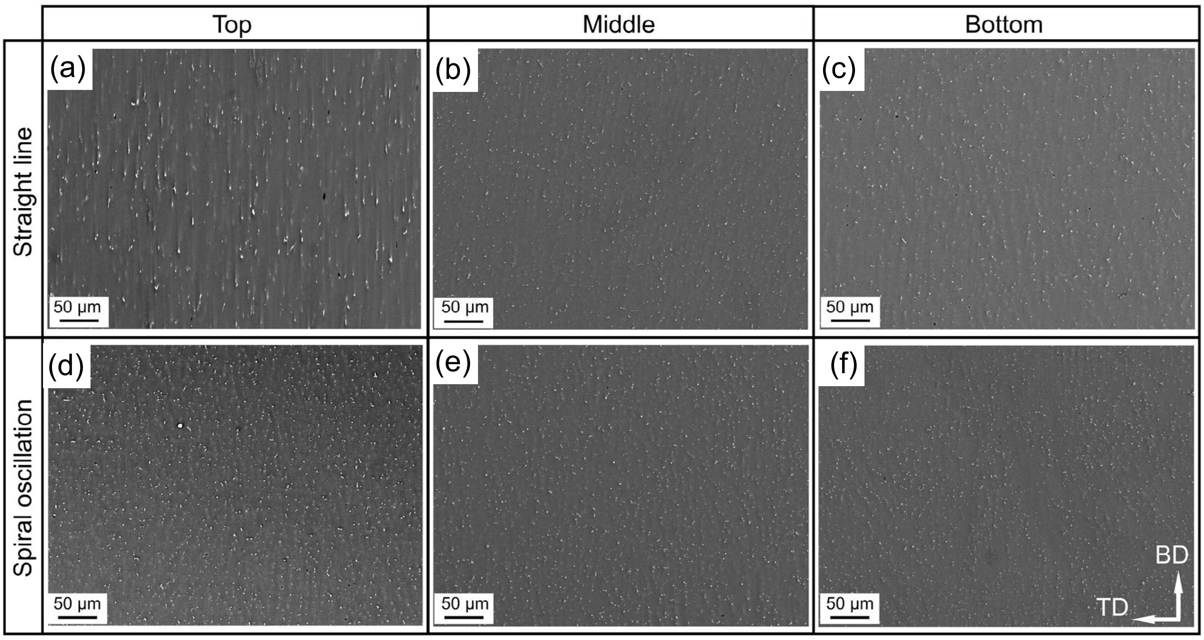

Fig. 7: SEM images of different positions in SL component (a–c) and SO component (d–f): (a, d) top; (b, e) middle; (c, f) bottom

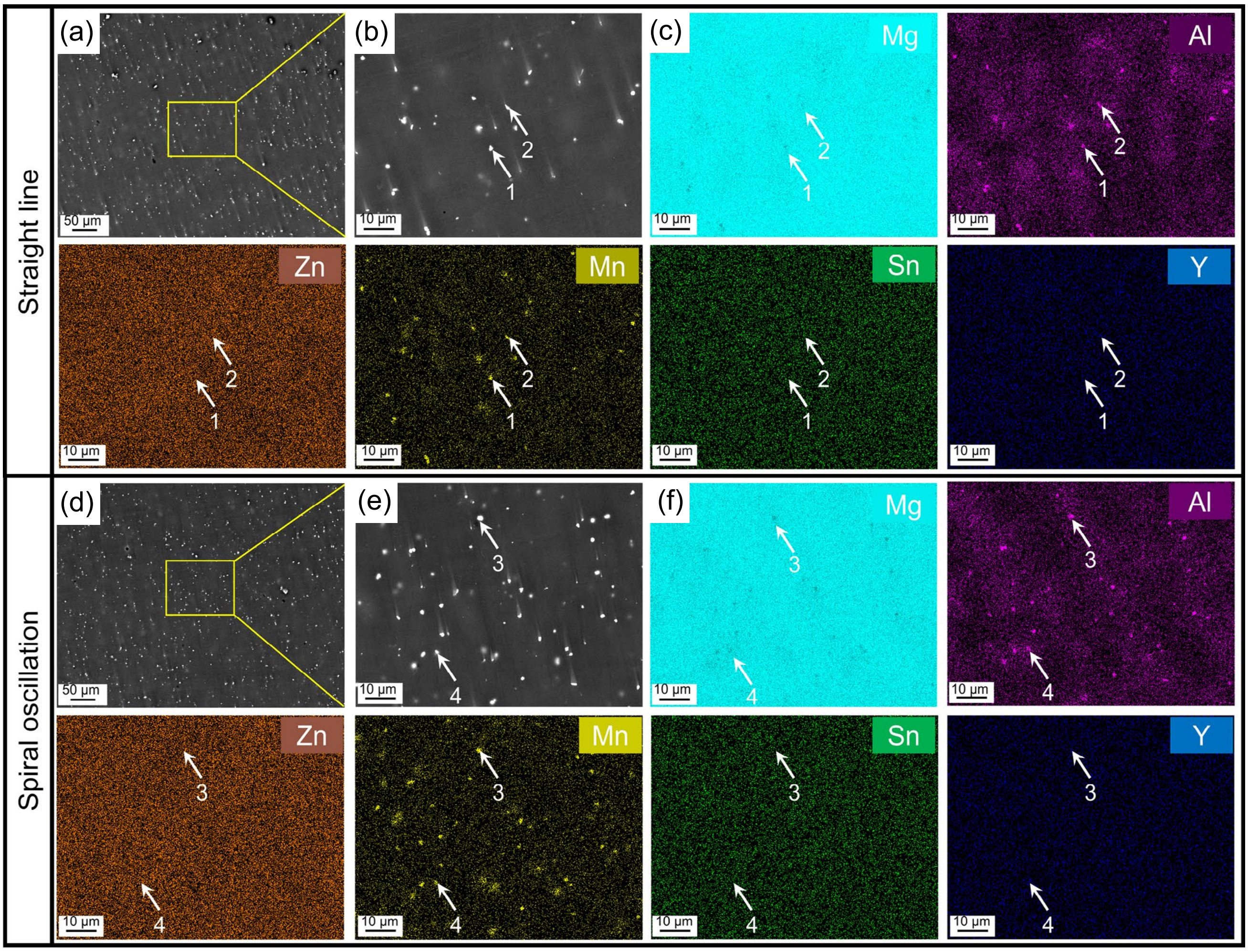

Fig. 8: SEM and EDS images of the middle region of the SL component (a–c) and SO component (d–f): (a, d) SEM; (b, e) locally magnified images corresponding to (a) and (d), respectively; (c, f) EDS images corresponding to (b) and (e), respectively

Table 1: Composition of second-phases, corresponding to points in Fig. 8 (at.%)

Point	Al	Mn	Zn	Sn	Y	Mg
1	4.65	2.25	0.16	0.03	0.01	Bal.
2	2.66	0.96	0.01	0.01	0.21	Bal.
3	2.47	1.24	0.16	0.02	0.01	Bal.
4	3.39	1.03	0.01	0.01	0.27	Bal.

determined by the ratio of growth rate to the temperature gradient (G/R), whereas grain size evolution is governed by their product ($G\times R$)[39]. The implementation of SO significantly reduces the temperature gradient, thereby increasing the degree of undercooling at the solidification front[37]. When the compositional undercooling exceeds the critical value required for nucleation, new equiaxed grains can heterogeneously nucleate on irregular particles at the solidification front. As these newly formed equiaxed grains grow, they hinder the further growth of columnar grains, facilitating the CET[40]. Consequently, the SO strategy results in a fundamentally different microstructure.

4 Conclusions

To promote the columnar-to-equiaxed transition, reduce mechanical anisotropy, and achieve simultaneous strength-ductility enhancement in WA-DED AZ31 Mg alloy, a SO strategy was implemented during deposition. Microstructures of SL and SO components were systematically investigated, and the effects of SO on grain morphology and size, texture intensity, second-phase distribution/composition and mechanical properties were comprehensively analyzed. Main conclusions are summarized as follows:

(1) The SO strategy significantly improves the mechanical performance of WA-DED AZ31 Mg alloy components, achieving a synergistic enhancement in both strength and ductility while reducing mechanical anisotropy. Taking the BD as an example, the YS, UTS, and EL of SL component are 92 MPa, 168 MPa, and 6.6%, respectively. In comparison, the SO component exhibits improved values of 101 MPa (YS), 232 MPa (UTS), and 16.3% (EL), representing increases of 9.7%, 38.1%, and 147%, respectively. Furthermore, the variance rates of YS, UTS, and EL between BD and DD decrease markedly from 3.4%, 14.3%, and 36.4% for SL component to 1.0%, 0.4%, and 0.6% for SO component,

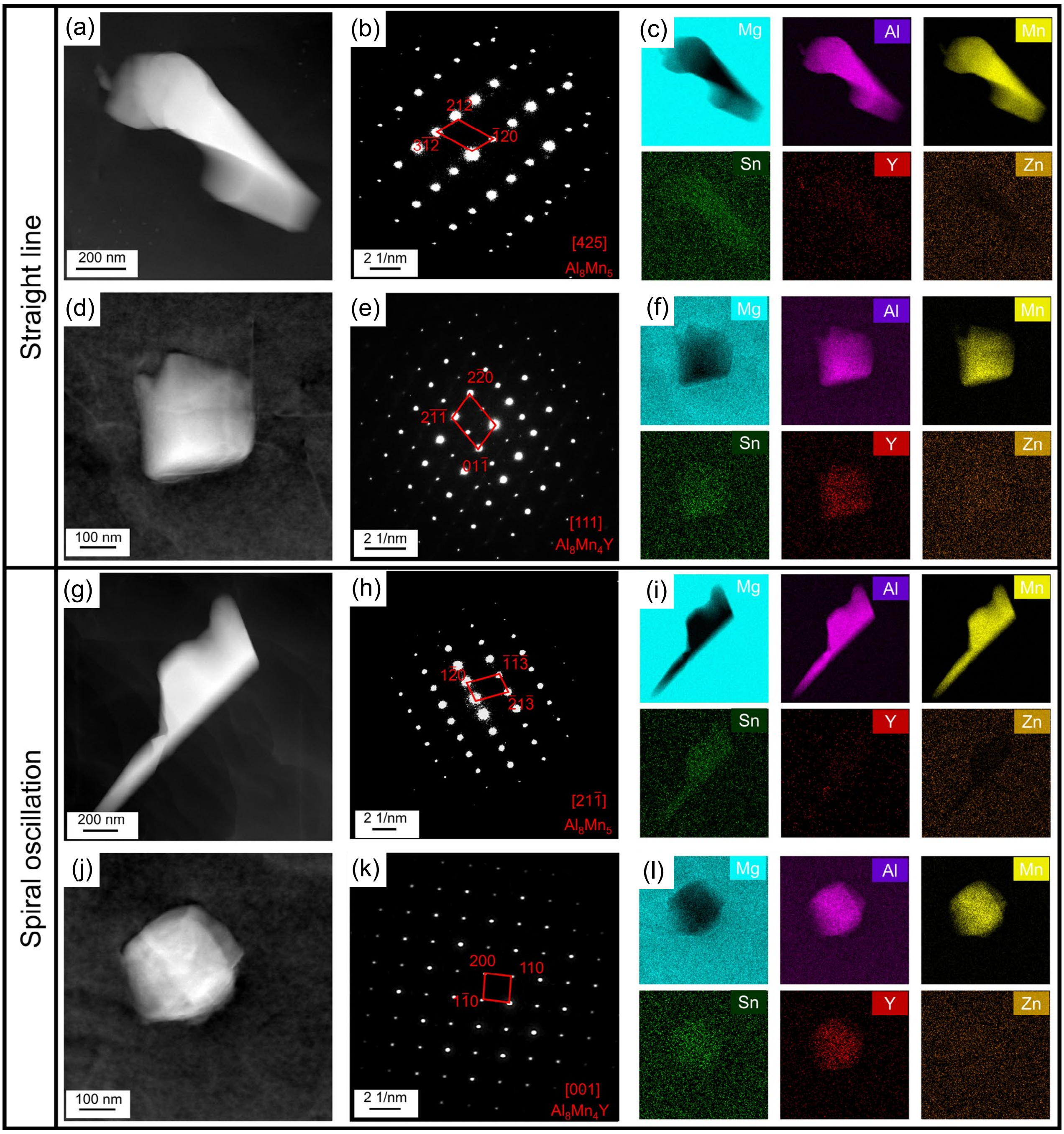

Fig. 9: TEM results of Al_8Mn_5 and Al_8Mn_4Y in SL (a)–(f) and SO (g)–(l) components: (a), (d), (g), and (j) high-angle annular dark-field (HAADF) images; (b), (e), (h), and (k) selected area electron diffraction (SAED) patterns, corresponding to (a), (d), (g), and (j), respectively; (c), (f), (i), and (l) EDS mapping results, corresponding to (a), (d), (g), and (j), respectively

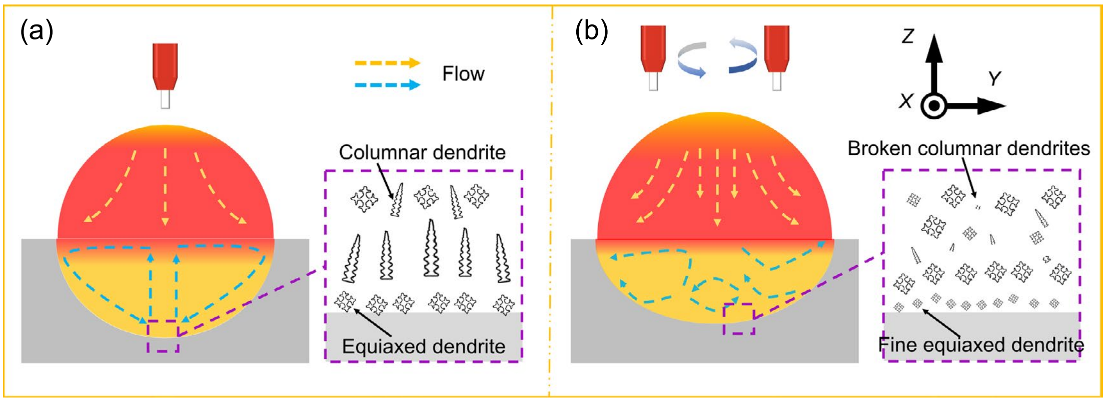

Fig. 10: Schematic for the flow field and grain structures in the molten pool of SL (a) and SO (b) components

indicating improved isotropy in mechanical properties.

(2) The SO strategy promotes CET, refines grains, and reduces the texture intensity. Specifically, taking the middle region between the SL and SO components as an example, the microstructure of SL component mainly consists of coarse columnar grains with an average grain size of 93.7 μm, while the SO component exhibits predominantly fine equiaxed grains with a reduced average grain size of 71.0 μm, corresponding to a 24.2% reduction (22.7 μm). Additionally, the maximum texture intensity is substantially decreased from 11.5 mrd in SL component to 2.9 mrd in SO component, with the latter showing more randomized grain orientations, which is favorable for enhancing isotropic mechanical behavior.

(3) The second-phase of both SL and SO components has a tendency to increase in size with increasing deposition heights. This is more pronounced in the SL component, which is mainly related to the change in heat dissipation conditions. The SO strategy promotes a more uniform distribution of second-phase particles, mitigating stress concentration and improving ductility. However, the chemical composition of second-phases remains unchanged. EDS analyses confirm that second-phase particles in both cases are Al_8Mn_5 and Al_8Mn_4Y.

Acknowledgments

This work was funded by the National Natural Science Foundation of China (Nos. 52334010 and 52001133), the Graduate Student Research Innovation Capability Enhancement Project of Jilin Province (No. JJKH20250101BS) and the Jilin Scientific and Technological Development Program (No. 20260205065GH).

Conflict of interest

The authors declare that they have no known competing financial interests or personal relationships that could have appeared to influence the work reported in this paper.

References

[1] Yang H, Chen X H, Huang G S, et al. Microstructures and mechanical properties of titanium-reinforced magnesium matrix composites: Review and perspective. Journal of Magnesium and Alloys, 2022, 10(9): 2311–2333.

[2] Kaushik V, Kumar B N, Kumar S S, et al. Magnesium role in additive manufacturing of biomedical implants – Challenges and opportunities. Additive Manufacturing, 2022, 55: 102802.

[3] Yang Y, Xiong X M, Chen J, et al. Research advances in magnesium and magnesium alloys worldwide in 2020. Journal of Magnesium and Alloys, 2021, 9(3): 705–747.

[4] Li K, Ji C, Bai S W, et al. Selective laser melting of magnesium alloys: Necessity, formability, performance, optimization and applications. Journal of Materials Science & Technology, 2023, 154: 65–93.

[5] Wang Y B, Ma B Q, Wang J X, et al. Quantitative analysis of columnar-to-equiaxed transition in Mg-Gd-Zn alloys. China Foundry, 2025, 22(3): 239–251.

[6] Zhou P C, You G Q, Feng J Y, et al. Mechanical properties and microstructures of Mg-6Si alloys fabricated using the tungsten-inert-gas arc additive manufacturing. China Foundry, 2025, 22(3): 263–272.

[7] Yang Y H, Guan Z P, Ma P K, et al. Wire arc additive manufacturing of a novel ATZM31 Mg alloy: Microstructure evolution and mechanical properties. Journal of Magnesium and Alloys, 2023, 12(12): 5024–5037.

[8] Fang X W, Yang J N, Jiang X, et al. Wire-arc directed energy deposited high-performance AZ31 magnesium alloy via a novel interlayer hammering treatment. Materials Science and Engineering: A, 2024, 889: 145864.

[9] Liu W, Jia H L, Zha M, et al. Superior strength-ductility synergy achieved in WA-DED Mg alloys by modulating precipitates through double-stage aging. Scripta Materialia, 2025, 267: 116819.

[10] Li X Z, Fang X W, Zhang Z Y, et al. Revealing precipitation behavior and mechanical response of wire-arc directed energy deposited Mg-Gd-Y-Zr alloy by tailoring aging procedures. International Journal of Extreme Manufacturing, 2024, 6(4): 045001.

[11] Li X Z, Fang X W, Fang D Q, et al. On the excellent strength-ductility synergy of wire-arc directed energy deposited Mg-Gd-Y-Zn-Zr alloy via manipulating precipitates. Additive Manufacturing, 2023, 77: 103794.

[12] Wu B T, Pan Z X, Ding D H, et al. A review of the wire arc additive manufacturing of metals: Properties, defects and quality improvement. Journal of Manufacturing Processes, 2018, 35: 127–139.

[13] Han S, Zielewski M, Martinez Holguin D, et al. Optimization of AZ91D process and corrosion resistance using wire arc additive manufacturing. Applied Sciences, 2018, 8(8): 1306.

[14] Li X Z, Zhang M G, Fang X W, et al. Improved strength-ductility synergy of directed energy deposited AZ31 magnesium alloy with cryogenic cooling mode. Virtual and Physical Prototyping, 2023, 18(1): e2170252.

[15] Guo Y Y, Quan G F, Jiang Y L, et al. Formability, microstructure evolution and mechanical properties of wire arc additively manufactured AZ80M magnesium alloy using gas tungsten arc welding. Journal of Magnesium and Alloys, 2021, 9(1): 192–201.

[16] Ma P K, Wang C, Jia H L, et al. Simultaneous enhancement in deposition efficiency and nano-scale precipitation of high-strength AZ31 Mg alloy via water cooling assisted wire-arc directed energy deposition. Thin-Walled Structures, 2025, 206: 112689.

[17] Wang P, Zhang H Z, Zhu H, et al. Wire-arc additive manufacturing of AZ31 magnesium alloy fabricated by cold metal transfer heat source: Processing, microstructure, and mechanical behavior. Journal of Materials Processing Technology, 2021, 288: 116895.

[18] Takagi H, Sasahara H, Abe T, et al. Material-property evaluation of magnesium alloys fabricated using wire-and-arc-based additive manufacturing. Additive Manufacturing, 2018, 24: 498–507.

[19] Li J W, Qiu Y M, Yang J J, et al. Effect of grain refinement induced by wire and arc additive manufacture (WAAM) on the corrosion behaviors of AZ31 magnesium alloy in NaCl solution. Journal of Magnesium and Alloys, 2023, 11(1): 217–229.

[20] Ying T, Zhao Z X, Yan P F, et al. Effect of fabrication parameters on the microstructure and mechanical properties of wire arc additive manufactured AZ61 alloy. Materials Letters, 2022, 307: 131014.

[21] Bao W Z, Qian B N, Yi H Q, et al. Enhancement of mechanical properties in AZ91D magnesium alloy via wire arc additive manufacturing: Influence of rapid solidification and solute segregation on microstructure and deformation behavior. International Journal of Plasticity, 2025, 190: 104376.

[22] Zhang C, Ju R F, Li Y L, et al. Wire-arc additive manufacturing of Mg-Gd-Y-Zn-Zr alloy: Microstructure and mechanical properties. Journal of Materials Research and Technology, 2024, 32: 3083–3092.

[23] Liu Z T, Wang L, Luo S Q, et al. Effect of heat treatment on microstructure and mechanical properties of WE43 alloy fabricated by wire arc additive manufacturing. Materials Today Communications, 2024, 41: 110950.

[24] Guo J, Zhou Y, Liu C M, et al. Wire arc additive manufacturing of AZ31 magnesium alloy: Grain refinement by adjusting pulse frequency. Materials, 2016, 9(10): 823.

[25] Fang X W, Yang J N, Wang S P, et al. Additive manufacturing of high performance AZ31 magnesium alloy with full equiaxed grains: Microstructure, mechanical property, and electromechanical corrosion performance. Journal of Materials Processing Technology, 2022, 300: 117430.

[26] Liu P W, Wang Z, Xiao Y H, et al. Insight into the mechanisms of columnar to equiaxed grain transition during metallic additive manufacturing. Additive Manufacturing, 2019, 26: 22–29.

[27] Yi H, Wang Q, Zhang W J, et al. Wire-arc directed energy deposited Mg-Al alloy assisted by ultrasonic vibration: Improving properties via controlling grain structures. Journal of Materials Processing Technology, 2023, 321: 118134.

[28] Li X Z, Fang X W, Zhang M G, et al. Gradient microstructure and prominent performance of wire-arc directed energy deposited magnesium alloy via laser shock peening. International Journal of Machine Tools and Manufacture, 2023, 188: 104029.

[29] Liu G, Su Y, Pi X Y, et al. Achieving high strength 316L stainless steel by laser directed energy deposition-ultrasonic rolling hybrid process. Materials Science and Engineering: A, 2024, 903: 146665.

[30] Liu G, Su Y G, Pi X Y, et al. Enhanced electrochemical corrosion resistance of 316L stainless steel manufactured by ultrasonic rolling assisted laser directed energy deposition. China Foundry, 2025, 22(2): 182–194.

[31] Yang Y H, Jia H L, Wang C, et al. An innovative strategy to prepare fine-grained Mg-Al alloys with a superior strength-ductility synergy via wire-arc directed energy deposition. Additive Manufacturing, 2024, 86: 104207.

[32] Liu M H, Liu R J, Long J Q, et al. Influence of oscillating laser on forming characteristics and molten pool flow behavior of aluminum alloy double-wire additive manufacturing. Journal of Laser Applications, 2023, 35(2): 022016.

[33] Chen C, Wang C J, Yang J L, et al. Enhanced strength-ductility synergy by promoting columnar-to-equiaxed transition and martensitic microstructure refinement with different laser oscillating strategies. Journal of Manufacturing Processes, 2024, 125: 164–175.

[34] Yu H H, Xin Y C, Wang M Y, et al. Hall-Petch relationship in Mg alloys: A review. Journal of Materials Science & Technology, 2018, 34(2): 248–256.

[35] Zhang Z, Xie J S, Zhang J H, et al. Towards designing high mechanical performance low-alloyed wrought magnesium alloys via grain boundary segregation strategy: A review. Journal of Magnesium and Alloys, 2024, 12(5): 1774–1791.

[36] Yuan T, Kou S, and Luo Z. Grain refining by ultrasonic stirring of the weld pool. Acta Materialia, 2016, 106: 144–154.

[37] Cheng S X, Liu F C, Xu Y, et al. Effects of arc oscillation on microstructure and mechanical properties of AZ31 magnesium alloy prepared by CMT wire-arc directed energy deposition. Materials Science and Engineering: A, 2023, 864: 144539.

[38] Wei Y H, Liu F C, Liu F G, et al. Effect of arc oscillation on porosity and mechanical properties of 2319 aluminum alloy fabricated by CMT-wire arc additive manufacturing. Journal of Materials Research and Technology, 2023, 24: 3477–3490.

[39] DebRoy T, Wei H L, Zuback J S, et al. Additive manufacturing of metallic components–Process, structure and properties. Progress in Materials Science, 2018, 92: 112–224.

[40] Yuan T, Luo Z, and Kou S. Grain refining of magnesium welds by arc oscillation. Acta Materialia, 2016, 116: 166–176.